Research Square

Preprints are preliminary reports that have not undergone peer review.
They should not be considered conclusive, used to inform clinical practice,
or referenced by the media as validated information.

Topological exceptional points bound in the continuum

Yong Li

yongli@tongji.edu.cn

Tongji University https://orcid.org/0000-0001-8049-9128

Jiachen Meng

Tongji University

Ruizhi Dong

Tongji University

Yihuan Zhu

Tongji University

Xu Wang

Tongji University https://orcid.org/0000-0001-5114-4897

Article

Keywords:

Posted Date: November 10th, 2026

DOI: https://doi.org/10.21203/rs.3.rs-11630306/v1

License: This work is licensed under a Creative Commons Attribution 4.0 International License.
Read Full License

Additional Declarations: There is **NO** Competing Interest.

Topological exceptional points bound in the continuum

Jiachen Meng[1], Ruizhi Dong[1*], Yihuan Zhu[1], Xu Wang[1*], Yong Li[1*]

[1]Institute of Acoustics, School of Physics Science and Engineering, Tongji University, No. 1239 Siping Road, Shanghai, 200092, China.

*Corresponding author(s). E-mail(s): ruizhi_dong@tongji.edu.cn; xuwang@tongji.edu.cn; yongli@tongji.edu.cn;

Abstract

The deliberate manipulation of symmetries has driven the discovery of exotic wave phenomena, most notably robust topological edge states (TESs), hypersensitive exceptional points (EPs), and zero-leakage bound states in the continuum (BICs). While pairwise combinations of these concepts have expanded the frontiers of wave control, unifying all three into a single hybrid state has remained elusive. Here, we conceptually and experimentally demonstrate a topological exceptional point bound in the continuum (TEP-BIC) utilizing an active acoustic metamaterial, uniquely governed by the fusion of crystalline, parity-time ($\boldsymbol{\mathcal{PT}}$), and local orthogonal spatial symmetries. By inducing $\boldsymbol{\mathcal{PT}}$ modulation to an acoustic lattice, we not only concurrently regulate band structure of distinct subspaces, decoupled from each other by mode orthogonality, but also drive paired TESs in one subspace to coalesce into an EP that is embedded within the extended bulk continuum of the other subspace. We experimentally demonstrate that these physical ingredients (TES, EP, and BIC) remain individually accessible even after being fused into a single state, uncovering its multifaceted nature that manifests as contrasting responses under different perturbations. This unity of topology, non-Hermitian degeneracy, and zero-leakage resonance unlocks a hybrid physical regime for wave manipulation, providing a promising pathway for ultra-sensitive, low-loss sensing devices.

1 Introduction

Symmetry dictates interaction, laying the foundation for the interplay between waves and matter and shaping their propagation across classical and quantum regimes [1–3]. Recent years have witnessed profound developments driven by the engineering of symmetry, accompanied by the discovery of exotic wave phenomena. In topological physics, discrete crystalline symmetries govern the emergence of global topological invariants, which in turn define distinct phases of matter [4–9]. This provides a global symmetry protection that endows localized modes (i.e. topological edge states, TESs) with strong robustness, rendering them intrinsically immune to backscattering and local perturbations. Moving beyond Hermitian bounds, exceptional points (EPs) emerge as spectral singularities that arise exactly at the spontaneous breaking of $\mathcal{PT}$ symmetry, inducing a dimensional collapse of eigenstates and yielding a drastically enhanced sensitivity [10–24]. Further, spatial symmetries enforce a strict decoupling from radiation/propagation modes, yielding completely localized resonances, known as symmetry-protected bound states in the continuum (BICs). BICs manifest perfect confinement, trapping waves even when embedded within a continuous spectrum of extended states capable of carrying energy away [25–31].

The fusion of these exotic states now is continuously pushing the boundaries of wave physics. Marrying topological protection with BIC confinement gives rise to topological BICs (TBICs), where the localized state embedded within the continuum is a TES [32–37]. This hybridization mitigates the inherent fragility of conventional BICs against fabrication imperfections, integrating the zero-leakage property of BICs with topological robustness. Meanwhile, the synergy of topology and non-Hermitian physics has brought about exceptional topological phases, reshaping the resulting wave dynamics [38–41]. Specifically, the introduction of non-Hermitian parameters (e.g., gain and loss) can force an original real TES to bifurcate into a complex conjugate pair, which subsequently coalesce at a critical threshold to form a topological exceptional point (TEP). Counterintuitively, the TEP embodies both strong immunity and high sensitivity, yielding a state that is globally shielded from structural disorder by topological invariants, yet sensitive to spectral perturbations. Finally, merging the non-radiating properties of BICs with the extreme sensitivity of EPs gives rise to exceptional bound states in the continuum (EP-BICs) [42, 43]. These hybrid non-Hermitian singularities uniquely emerge when multiple BICs are driven to coalesce into a single state. By simultaneously inheriting the zero-leakage confinement of a BIC and the dramatic perturbation response

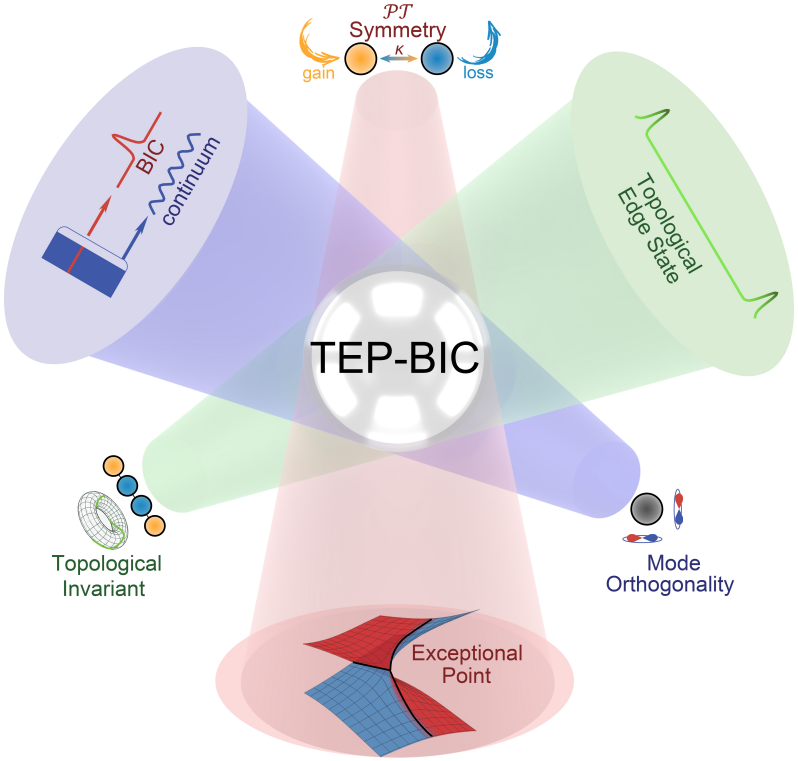


Fig. 1 Concept of topological exceptional points bound in the continuum (TEP-BICs). The schematic summarizes the fusion of topological edge states, non-Hermitian exceptional points, and symmetry-protected bound states in the continuum. Even after being unified into a single hybrid state, these physical signatures remain independently observable through distinct yet complementary channels.

of an EP, EP-BICs provide a promising pathway for ultra-sensitive, low-loss sensing devices. Yet, despite these profound pairwise advancements, thus far, an integration of all three—topology, BICs, and EPs—remains elusive.

Here, we conceptually propose and experimentally observe one of the first topological exceptional point bound in the continuum (TEP-BIC). To demonstrate our approach, we take a conceptually simple metamaterial structure, governed by the fusion of discrete crystalline, parity-time, and local orthogonal spatial symmetries (Fig. 1). At the fundamental unit-cell level, the system supports two distinct modes, where the local-symmetry-induced mode orthogonality guarantees their complete decoupling. Extended into a crystalline lattice, these modes develop independent band structures, enabling the coexistence of continua without hybridization. Topology is subsequently introduced through a non-Hermitian acoustic analog of a generalized SSH model via band folding, where the topological phase transition is driven solely by non-Hermiticity—by introducing a balanced gain and loss distribution to form a four-unit $\mathcal{PT}$-symmetric supercell. Consequently, TESs emerge in pairs in the complex frequency domain, for both decoupled mode subspaces. By $\mathcal{PT}$ modulations, we not only regulate band structure of both subspaces, but also drive the paired TESs in one subspace to coalesce into an EP (i.e. TEP), embedding this TEP into the extended bulk continuum of the orthogonal subspace. Remarkably, even after being fused into a single hybrid state, the physical ingredients remain independently observable through distinct yet complementary channels (conceptually illustrated in Fig. 1). These results establish a general route for organizing and resolving topology, radiation confinement, and exceptional singularity into a unified physical framework.

2 Results

To establish the theoretical framework of the TEP-BIC, we begin by considering an ideal one-dimensional tight-binding model (Fig. 2a). The fundamental building block is a meta-atom supporting two on-site states belonging to distinct spatial symmetries—denoted as σ and π modes, spectrally separated by an on-site frequency detuning $\Delta\omega$. When these meta-atoms are arrayed into a periodic lattice, their localized states hybridize into continuous Bloch bands separated by stop bands. Dictated by their differing spatial symmetries, σ and π modes exhibit different nearest-neighbor hopping (κ_σ and κ_π), evolving into independent band structures within their respective subspaces, where mode orthogonality guarantees they remain decoupled. We subsequently introduce non-Hermiticity into the lattice by configuring every four meta-atoms into a supercell with a balanced gain-loss profile with modulation strength γ (Fig. 2a), rendering the system $\mathcal{PT}$-symmetric. Consequently, taking the σ mode as an example, the on-site states in a supercell manifest in a paired form: depending on the strength of the non-Hermitian modulation, these paired states appear in terms of either $\sigma \pm \gamma$ or complex conjugate $\sigma \pm i\gamma$, corresponding to the $\mathcal{PT}$-symmetric and $\mathcal{PT}$-broken regimes, respectively. Such $\mathcal{PT}$-modulation-induced tetramerization effectively folds the Brillouin

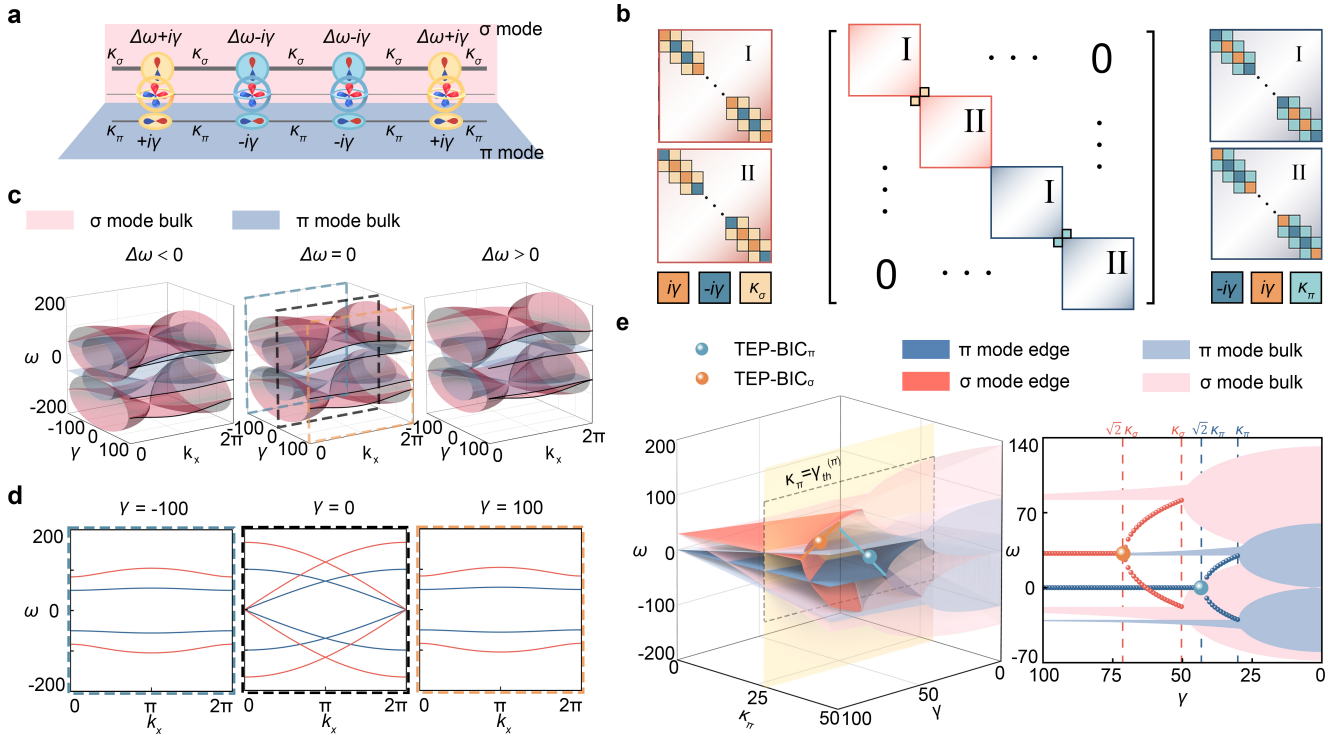


Fig. 2 Theoretical framework for constructing TEP-BICs. a, Schematic of the one-dimensional tight-binding lattice model. The system supports symmetry-distinct mode subspaces (σ and π) governed by mode-dependent couplings and a balanced gain–loss modulation profile. **b**, Block representation of the effective Hamiltonian. The full system is formed by interfacing two topologically nontrivial and inequivalent lattices (configurations I and II). The Hamiltonian encompasses both subspaces. **c**, Concurrent complex-band evolution of both subspaces as a function of the non-Hermitian modulation strength γ, evaluated at representative frequency detunings $\Delta\omega < 0$, $\Delta\omega = 0$, and $\Delta\omega > 0$. **d**, Momentum-resolved band structures at $\gamma = -100$, 0, and 100, corresponding to the three cross-sectional slices extracted from the middle panel in **c**. **e**, Eigenfrequency evolution in the (γ, κ) parameter space for a finite-size system constructed by interfacing the two inequivalent lattices. A representative constant-κ cross-section is presented alongside, with colored markers highlighting the exceptional degeneracies of the paired topological edge states.

zone, paving the way for the emergence of topological phase. This enables the construction of two topologically non-trivial but mutually inequivalent lattices (setting the central two with gain and the outer two with commensurate loss, or vice versa), where their interface acts as a domain wall that guarantees the emergence of localized TESs.

Mathematically, the effective Hamiltonian of the whole system can be expressed in a block form (see Supplementary Secs. 1 and 2 for the theoretical model and Hamiltonian representations). The middle part of Figure 2b shows the Hamiltonian of the whole system, while the left and right parts illustrate the blocks belonging to the two subspaces (σ and π, distinguished by different background shadings), featuring distinct mode-dependent couplings κ_σ and κ_π. The imaginary terms $\pm i\gamma$ describe the introduced balanced gain–loss modulation. For each subspace, configurations I and II correspond to distinct non-Hermitian topological phases (distinguished by the inverted arrangement of the diagonal entries in the blocks), and their interface supports paired TESs. Figure 2c depicts the concurrent band evolution of both subspaces with the varying non-Hermitian parameter γ at different detuned frequency $\Delta\omega$ under periodic boundary conditions. Varying $\Delta\omega$ shifts the relative spectral positions of the σ and π mode bands, allowing them to spectrally overlap and coexist. Figure 2d further illustrates the band structures at $\Delta\omega = 0$ for three representative values of γ, corresponding to three slices extracted from the middle panel of Fig. 2c. Notably, the middle panel of Fig. 2d witnesses the degeneracy of two Dirac points (DPs) when the detuned frequency $\Delta\omega$ diminishes. Although degenerated at the same frequency, the two DPs possess different eigenstates, belonging to distinct symmetric subspaces and fully decoupled with each other. The non-Hermitian parameter γ opens the gaps, continuously reorganizing the band structure and driving the associated band inversion, which gives rise to a topological phase transition and forms non-trivial yet topologically inequivalent lattices on opposite sides of $\gamma = 0$ (see details in Supplementary Sec. 3). Remarkably, as illustrated in Fig. 2d, these representative band structures show not merely a band evolution in spectra but also a change in band multiplicity in the real frequency plane (the number of bands prior to the non-Hermitian modulation being double that of the topologically non-trivial lattices after γ is introduced), which stands as a hallmark of the unique topological phase transition driven solely by non-Hermitian modulation.

To characterize the topology induced by non-Hermitian modulation, we calculate the non-Abelian Wilson loop of the relevant band subspace [44]. The resulting Wilson-loop invariant takes a quantized value of 1/2 for the two selected lattices at $\gamma = \pm 100$, identifying their non-trivial non-Hermitian topological phases. When these two topologically inequivalent but spectrally identical lattices are joined together, their interface naturally forms a domain wall. Physically, the emergence of TES at the domain wall is governed by the competition between the non-Hermitian modulation strength γ and the inter-site coupling κ. By matching the evanescent solutions on the

two sides of the domain wall, the decay factor β of the interface mode satisfies (see details in Supplementary Sec. 4)

$$\beta + \beta^{-1} = 4\left(\frac{\gamma}{\kappa}\right)^2 - 2. \tag{1}$$

For $\gamma < \kappa$, we have $|\beta| = 1$, so the corresponding solutions remain extended, merging with the bulk spectrum. Once $\gamma > \kappa$, one of the two solutions becomes

$$\beta_{\text{int}} = \left[\frac{\gamma}{\kappa} - \sqrt{\left(\frac{\gamma}{\kappa}\right)^2 - 1}\right]^2 < 1, \tag{2}$$

yielding a pair of states localized at the domain wall, with one exponentially growing and the other exponentially decaying. Consequently, the number of TESs increases from two (localized at the outer boundaries of the whole system) to four (owing to the emergence of an additional pair at the central domain wall). Notably, the two mode sectors (σ and π) reach this topology transition at different values of γ because of their different coupling strengths. Consider the coupling strength of mode σ to be approximately twice that of π sector (specifically chosen to match our subsequent realization). Accordingly, the π mode TESs at the interface emerge first as γ increases. As highlighted by the right panel of Fig. 2e, the π mode TESs start to separate from the bulk spectrum when $\gamma_{\text{th}}^{(\pi)} = \kappa_\pi$; while, by contrast, the stronger coupling of the σ sector yields a higher threshold at $\gamma_{\text{th}}^{(\sigma)} = \kappa_\sigma$. The different onset thresholds therefore reflect the mode-dependent competition between non-Hermitian modulation and inter-cell coupling.

In the following, we focus exclusively on the paired TESs pinned at the domain wall, as they eventually degenerate into the TEP-BIC; whereas the remaining two TESs, respectively confined to the opposite outer boundaries of the whole system, cannot form a degeneracy. Solving the interface matching condition further gives the two interface TESs' eigenvalues as

$$\omega_\pm = \pm\sqrt{2\kappa^2 - \gamma^2}. \tag{3}$$

Thus, in the regime $\kappa < \gamma < \sqrt{2}\kappa$ ($\kappa < \gamma$ being the prerequisite for the emergence of these TESs), the paired TESs remain spectrally separated, with their spectral splitting continuously collapsing as γ approaches $\sqrt{2}\kappa$ until the eigenvalues eventually coalesce at $\omega = 0$, accompanied by the simultaneous merging of their corresponding eigenvectors (the signature of a second-order EP). Upon further increasing the non-Hermitian modulation ($\gamma > \sqrt{2}\kappa$) the system transitions from the $\mathcal{PT}$-symmetric into the $\mathcal{PT}$-broken regime, with the two eigenvalues bifurcating in the imaginary frequency plane as

$$\omega_\pm = \pm i\sqrt{\gamma^2 - 2\kappa^2}. \tag{4}$$

Intriguingly, because this entire evolution occurs within the subspace of σ, the coalescing TESs retain their suppressed coupling to the propagation continuum of subspace π. The different-colored dots in Fig. 2e mark the degenerate points of the paired TESs of σ and π in the parameter space (γ, κ, ω); while the right panel—a slice at a fixed κ—resolves the details of the emergence and coalescence of these paired TESs into TEPs, which are mutually embedded within the orthogonal bulk continua to form their respective TEP-BICs (see Supplementary Sec. 5 for the band evolution details). The resulting state therefore simultaneously exhibits TES localization, BIC confinement, and EP degeneracy. Notably, as the non-Hermitian modulation increases, the transition across the EP dictates not only the coalescence of the split TESs into degeneracy, but also a simultaneous, drastic compression of the bulk bandwidth (Fig. 2e).

Mapping this idealized tight-binding theoretical model onto a physical platform, we construct an acoustic lattice consisting of cavities coupled through connecting necks (see Supplementary Sec. 6, Fig. S4, and Table S1 for the geometric parameters of the physical structure). For each four-cavity supercell, by equipping the two central and the two outer cavities with balanced gain (Fig. 3a, yellow) and loss (blue) respectively, or vice versa, we establish two distinct configurations with topologically inequivalent non-trivial phases. Each supercell supports two symmetry-distinct intracavity modes, σ and π, whose pressure fields exhibit different parity distributions (Fig. 3a, the bottom panel). For this platform, the mode symmetries enforce inter-subspace decoupling which is the basis for BIC, whereas the gain/loss imparts the $\mathcal{PT}$ modulation responsible for generating the TESs and driving their coalescence into an EP. Here, the cavity dimensions l_x and l_y provide independent degrees of freedom to control the spectral positions of the two modes; while their difference Δl not only modulates $\Delta\omega$, providing an effective tuning mechanism to shift the relative positions of the two band structures, but also modulates the coupling, κ_σ and κ_π (see detailed discussion in Supplementary Sec. 7).

Figure 3b shows the evolution of the σ mode TESs in the complex frequency space under non-Hermitian modulation. As the normalized gain–loss modulation $\Delta\gamma/\gamma$ is varied, the eigenfrequencies of the paired TESs undergo a typical $\mathcal{PT}$-symmetry breaking transition—switching from real-part to imaginary-part splitting across the degenerate point, confirming the coalescence of TESs at the crossing as a TEP. Concurrently, the geometric detuning Δl shifts the relative spectral positions of the σ and π modes, giving rise to distinct regimes characterized by the coexistence and spectral overlap of edge and bulk states (Fig. 3c). Here, the light pink and light blue states correspond to the σ and π bulk modes, respectively, whereas the red and blue dots identify their associated TESs. At $\Delta l = -0.32$ mm, the degenerate TESs of σ are tuned to be spectrally embedded within the extended bulk

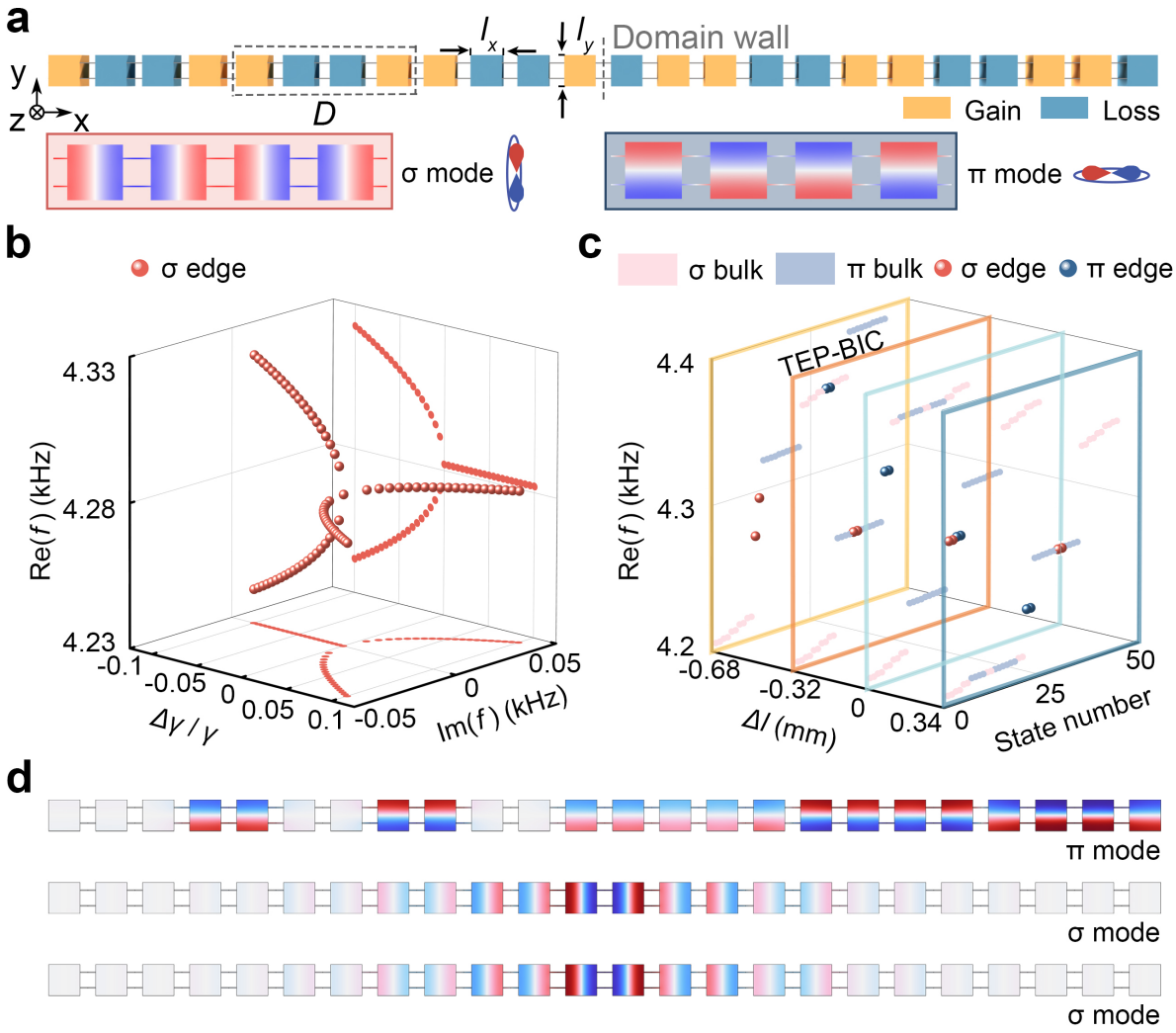


Fig. 3 Numerical realization of the TEP-BIC in an acoustic $\mathcal{PT}$ cavity lattice. a, Schematic of the acoustic system constructed by interfacing two topologically inequivalent finite-size lattices. Both lattices are composed of four-cavity supercells hosting the symmetry-distinct σ and π intracavity modes, with gain and loss cavities indicated in yellow and blue, respectively. The interface between these two lattices establishes a domain wall that supports the TEP-BIC. **b**, Evolution of the complex eigenfrequencies for the σ mode topological edge states as a function of the normalized non-Hermitian modulation $\Delta\gamma/\gamma$, illustrating their coalescence at an exceptional point. **c**, Eigenspectra of the finite-size system evaluated at representative geometric detunings Δl, revealing the coexistence and spectral overlap of the localized edge and extended bulk states of both σ and π. **d**, Spatial field distributions of the system eigenstates at the TEP-BIC frequency. The π mode manifests as a spatially extended bulk state, whereas the two σ modes are localized at the domain wall, exhibiting identical field profiles that confirm their exact degeneracy.

continuum of the orthogonal π sector. Figure 3d further presents the pressure-field distributions for all eigenstates at the specific frequency of the TEP-BIC. In contrast to the eigenstate of π showing the extended nature of bulk, the two eigenstates of σ are strongly localized at the interface, manifesting the paired TESs. Notably, these two TESs exhibit identical spatial mode profiles, signifying that they are degenerate not only in frequencies but also in their states. Together, this unique configuration—an EP born from the coalescence of TESs, embedded within yet strictly decoupled from a continuous bulk spectrum——constitutes the realization of our TEP-BIC.

We construct an experimental prototype based on an active acoustic cavity array (see Methods Sec. 4.3 for experimental implementation and measurements). Figure 4a illustrates the fundamental cavity unit. To make a gain unit, effective gain is introduced into the cavity via an active microphone–speaker feedback loop (see details about the feedback loop in Supplementary Sec. 8); alternatively, a lossy unit is realized by inserting absorbing foam. For both units, an additional speaker and microphone are employed for local excitation and response measurements. Notably, to enable mode-selective operation and feedback, each cavity is engineered with two distinct sets of ports specifically targeting the orthogonal σ and π modes. During each measurement, only the ports corresponding to the target mode are utilized, while the unused set is sealed with custom-designed plugs. In experiments, the effective gain is tuned by adjusting the feedback coefficient, while the effective loss is controlled by varying the thickness of the inserted absorbing foam. To calibrate these two forms of non-Hermitian modulation (gain and loss), we first configure an isolated pair of gain and loss units. These cavities are equipped with two additional orthogonal arrays of probing ports at the top (Fig. 4a) to map the spatial profiles of the respective modes, allowing us to extract the acoustic pressure distribution, i.e., Re(p), inside the cavity. For the three distinct cavity configurations—the gain, loss, and unmodulated reference cavities, the experimental measurements exhibit good agreement with the simulations (Fig. 4a, the right panel). Importantly, compared to the reference cavity, the introduction of gain and loss merely scales the amplitude of pressure (amplifying or attenuating in equal proportions) without distorting

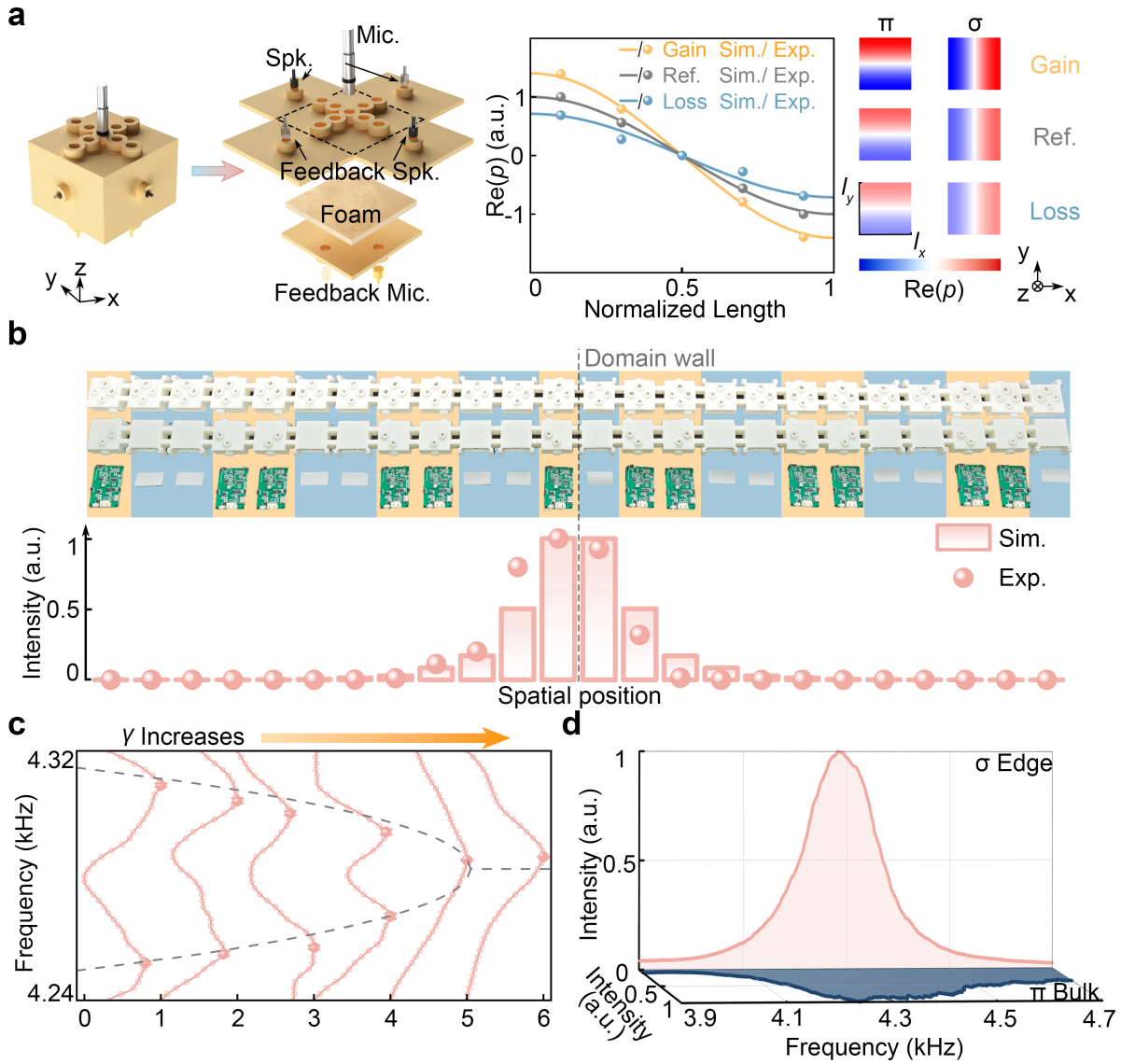


Fig. 4 Experimental realization and characterization of the TEP-BIC. a, Schematic of the basic cavity unit. Effective gain is introduced via an active microphone-speaker feedback loop, whereas effective loss is implemented by inserting an absorbing foam layer. An additional pair of speaker and microphone is utilized for local excitation and detection. These transducers can be mounted at two distinct port locations to selectively address the σ and π modes. Two orthogonal sets of probing ports on the cavity top are used to map the intracavity acoustic field distributions for both modes, with all idle ports sealed by custom-designed plugs. The right panel displays the measured intracavity field profiles for the gain, loss, and reference units, and their characteristic modal distributions. **b**, The 24-cavity experimental lattice, formed by interfacing three four-cavity supercells on either side of the domain wall. The bottom panel traces the measured spatial pressure distribution of the σ mode TES along the lattice. **c**, Acoustic pressure spectra measured in the gain cavity at the domain-wall across different non-Hermitian modulation strengths γ. **d**, Mode-selective spectral characterization of the localized σ mode edge state alongside the coexisting π mode bulk continuum.

the original acoustic field profile in the cavity. This ensures that the applied non-Hermitian modulations do not compromise the intrinsic modal symmetries, which is an important prerequisite for establishing the BIC. Using these cavities with independently controlled gain and loss, we assemble the finite lattice shown in Fig. 4b. The experimentally realized entire array comprises 24 units—12 lossy cavities with absorbing layers and 12 active cavities driven by local active feedback, where every four units constitute a designed supercell. Specifically, the left and right topologically inequivalent lattices each contain three supercells, with their interface establishing a central domain wall (see Supplementary Sec. 9 for cases with a larger number of supercells). Prior to each measurement, we perform a site-by-site calibration on each cavity across the entire array, ensuring that the internal sound pressure remains strictly uniform across all gain and loss cavities, respectively, as depicted in the right panel of Fig. 4a.

To experimentally verify the TES characteristic, we first map the spatial distribution of the intracavity acoustic field across all units in the lattice (Fig. 4b). Upon applying an excitation at the center of the array, the local acoustic pressure is sequentially recorded by a probe microphone embedded within each unit. The measured amplitudes, normalized to the peak pressure, reveal a localized spatial profile: the acoustic field exhibits a pronounced enhancement at the domain wall and decays exponentially outward across the entire lattice (see the corresponding numerical spatial comparison in Supplementary Sec. 10). The EP behavior is then examined by varying the non-Hermitian strength γ and measuring the spectral response of the central gain cavity. At relatively small γ, the spectrum of the gain cavity exhibits two well-resolved peaks, corresponding to the paired TESs (leftmost profile in Fig. 4c). As γ is gradually increased, the two TESs progressively move towards one another and coalesce,

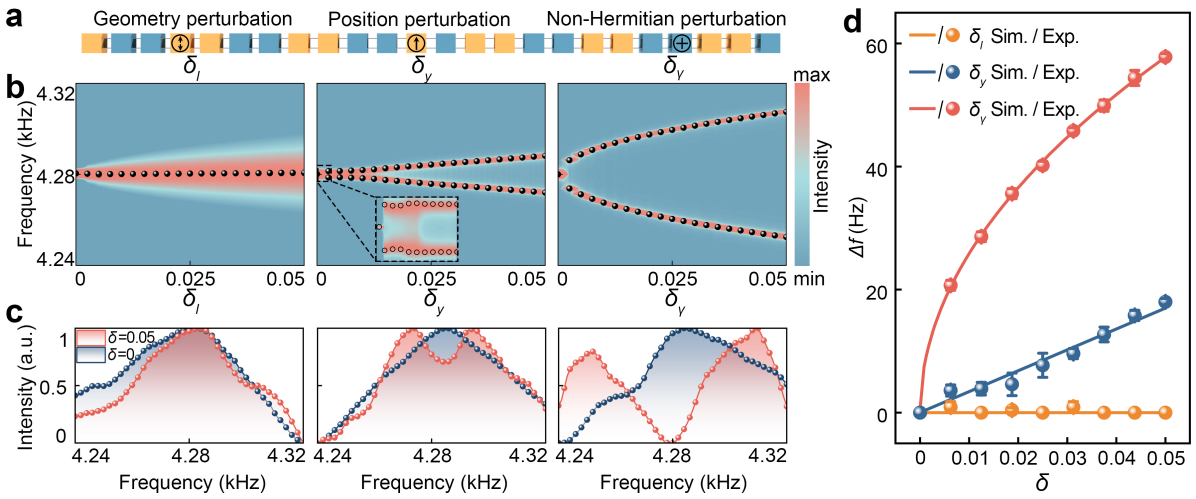


Fig. 5 Experimental observation of the multifaceted nature of the TEP-BIC. a, Schematics illustrating the three distinct types of perturbations applied to the system: cavity geometry perturbation δ_l, cavity position perturbation δ_y, and non-Hermitian perturbation δ_γ. **b**, Simulated spectral evolution of the system under these three respective perturbations. The color maps represent the field intensity evaluated at the domain-wall gain cavity, while the superimposed dots pinpoint the spectral trajectories of the eigenstates. **c**, Measured acoustic spectra probed at the domain-wall gain cavity before and after introducing the three perturbations at representative strengths. **d**, Frequency splitting Δf of the paired topological edge states as a function of the varying perturbation strengths.

marking the formation of the EP. With a further increase in γ, the system enters the $\mathcal{PT}$-broken regime, where the frequencies (i.e. the real parts of the eigenvalues) of the TESs remain degenerate. We finally investigate the BIC feature by comparing the acoustic responses under mode-selective excitation configurations. Specifically, to isolate the σ mode, the excitation speaker of the gain unit at the domain wall is mounted at the side-wall port aligned with one direction (the x-direction in Fig. 4d), with the probe microphone correspondingly oriented at the cavity bottom. Under this localized excitation, a pronounced peak corresponding to the σ mode TES is observed near 4.3 kHz within the same cavity, matching the simulation predictions in Fig. 3d. Subsequently, we probe the orthogonal π mode within the same frequency range. By reorienting the source and receiver to the perpendicular ports, we selectively couple to the π mode. To capture its nature as a propagating bulk state, we relocate the excitation source to a distant unit (seven units away from the measurement site). The measurements reveal the spectrally coexisting bulk modes of the π sector (Fig. 4d). The embedding of the localized state within the bulk continuum thus confirms the existence of a BIC. Together with the TES feature observed in Fig. 4b and EP characteristics observed in Fig. 4c, these measurements collectively establish the experimental demonstration of a TEP-BIC, in which topological localization, exceptional degeneracy, and propagation decoupling coexist within a single acoustic system.

TES, EP, and BIC represent three distinct and exotic physical states; their fusion endows this hybrid state with a multifaceted nature. We introduce three distinct perturbations that selectively probe these ingredients, namely, geometry perturbation δ_l, position perturbation δ_y, and non-Hermitian perturbation δ_γ (Fig. 5a). Physically, δ_l modifies the unit geometries while globally preserving the lattice symmetry (i.e. periodicity) underlying the topology; δ_y breaks the modal-symmetry condition responsible for the radiation decoupling; and δ_γ modulates the gain–loss contrast to perturb the system around non-Hermitian degeneracy. These perturbations provide three complementary channels for resolving the TES, BIC and EP characteristics of the established state, as conceptually illustrated in Fig. 1 (see Supplementary Sec. 11 for the detailed perturbation configurations). Under perturbation δ_l, the eigenfrequency of the TEP-BIC of the lattice remains unchanged across the investigated parameter range, reflecting the robustness afforded by the topological protection (Fig. 5b, the left panel). Conversely, the lateral shift δ_y breaks the symmetry-protected modal decoupling and lifts the strict BIC condition, leading to the abrupt collapse of the true BIC state (detailed in the zoomed-in inset of Fig. 5b, note the sharp color transition at the onset). Consequently, the originally decoupled π mode bulk hybridizes with the localized σ mode edge, giving rise to two new quasi-BIC modes that exhibit a linear spectral splitting as δ_y increases (the middle panel of Fig. 5b). In contrast, the introduction of the non-Hermitian perturbation δ_γ yields a distinct outcome: the hypersensitivity rooted in the EP endows the system with a strong response, characterized by the square-root spectral splitting.

The above three distinct responses are also observed experimentally (see Supplementary Secs. 12 and 13 for the experimental setup and complete measured spectra), by comparing the measured spectra before and after applying a representative perturbation. For the perturbation in δ_l, the position of the spectral peak remains virtually unshifted (Fig. 5c, the left panel). Meanwhile, breaking the BIC-protecting symmetry produces a resolvable splitting of the resulting quasi-BICs (the middle panel). When the non-Hermitian potential is perturbed, the initially coalesced response splits into two well-separated peaks. To quantitatively evaluate these behaviors of the TEP-BIC, we systematically apply perturbations with varying magnitudes. In Fig. 5d, the resulting frequency splitting, Δf, is plotted as a function of the normalized perturbation strength. Benefiting from topological protection, the state exhibits robustness against δ_l, maintaining its frequency invariant and without splitting as the perturbation

increases. In contrast, breaking the spatial symmetry (δ_y) dismantles the BIC condition and yields a moderate increase in the spectral separation, demonstrating a linear sensitivity (note that this linear response characterizes the quasi-BIC modes, as the true BIC is instantly annihilated upon the introduction of δ_y). Conversely, the non-Hermitian perturbation (δ_γ) triggers a strong response even at small perturbation values, illustrating an enhanced sensitivity that follows the square-root scaling characteristic of a second-order EP. Collectively, the measured data reproduce these distinct scaling trends, revealing a clear sensitivity hierarchy among the TES, BIC, and EP facets within this single state. The agreement between experiment and simulation validates our experimental strategy as a powerful means to selectively probe the three physical ingredients of the TEP-BIC (see Supplementary Sec. 14 for additional numerical results under different disorder realizations).

3 Conclusion

To conclude, we have theoretically proposed and experimentally realized a hybrid state as the fusion of TES, EP, and BIC within a single active acoustic array, achieved by engineering $\mathcal{PT}$ modulation via local active feedback and passive absorbing materials. While a simple pair of $\mathcal{PT}$-symmetric coupled cavities can host a conventional EP, we demonstrate that a lattice of such cavity pairs can support a topological EP—arising from the degeneracy of a TES pair—which can be further engineered to embed within the bulk continuum as a BIC. Founded upon the coexistence of discrete translational, parity-time, and local orthogonal spatial symmetries, this hybrid state exhibits a multifaceted nature, unifying topological localization, symmetry-protected propagation decoupling, and exceptional degeneracy. Our experimental observations uncover a clear hierarchy of these multifaceted responses: robustness against structural disorder (δ_l), a linear sensitivity of mode-symmetry-broken (δ_y), and an amplified sensitivity native to the non-Hermitian perturbation (δ_γ). Such contrasting responses observed under different perturbations further imply that these physical ingredients remain individually addressable, even after being fused into a single state. The unity of TES, EP, and BIC unlocks new degrees of freedom for wave manipulation, presenting a unique solution to integrate distinct sensitivities—linear and square-root, which mutually complement each other by offering advantages under large and minute perturbations, respectively—alongside topological protection. These findings may broaden the horizons of non-Hermitian wave physics, offering a robust theoretical and experimental foundation that can be readily extended to photonics, mechanics, and other artificial structured materials for advanced wave manipulation and sensing applications.

4 Methods

4.1 Topological and exceptional-point calculations

The non-Hermitian band topology was characterized using biorthogonal Wilson loops. For the Bloch Hamiltonian, the left-eigenvector basis was constructed from the right-eigenvector matrix as $V_L(k) = [V_R^{-1}(k)]^\dagger$. Within the selected two-band subspace, the overlap matrices $F_{mn}(k_i, k_{i+1}) = \langle u_m^L(k_i) | u_n^R(k_{i+1}) \rangle$ define the Wilson loop $W = \prod_i F(k_i, k_{i+1})$, whose eigenvalues λ_j yield the Wannier centers $\nu_j = -i \ln \lambda_j / (2\pi)$. Interface states were identified from the localized eigenmodes of a finite domain-wall lattice. A second-order exceptional point occurs when their eigenvalues and eigenvectors coalesce at $\gamma = \sqrt{2}\kappa$. The BIC condition was verified by spectral embedding within, and symmetry-protected decoupling from, the orthogonal bulk sector. Further derivations are provided in Sections 1, 4, and 5 of the Supplementary Information.

4.2 Numerical simulations

Finite-element calculations were performed in finite-element simulation software using Eigenfrequency and Frequency Domain studies. Air properties were $\rho_0 = 1.21\,\mathrm{kg\,m^{-3}}$, $c_0 = 343\,\mathrm{m\,s^{-1}}$, and $\mu = 1.81 \times 10^{-5}\,\mathrm{N\,s\,m^{-2}}$. Bloch periodic conditions were applied to calculate bulk bands, whereas finite lattices were used to resolve interface eigenstates and pressure fields. The σ and π modes were distinguished by their spatial parity, and their geometric dependence was obtained by linear fitting. Frequency-domain simulations reproduced the experimental excitation and detection configurations.

4.3 Experimental implementation and measurements

The 24-cavity lattice was fabricated by stereolithography with a nominal precision of 0.1 mm. Gain was implemented using local microphone–loudspeaker feedback with an analog signal path and digitally adjustable gain; loss was introduced using absorbing foam. The units were calibrated before assembly to confirm preservation of modal parity. A separate source excited the lattice, and responses were recorded using a GRAS 46BD microphone and a National Instruments PXIe-4431 module. Frequency sweeps, spatial scans, and mode-selective measurements characterized the edge-state spectra, localization, and coexisting bulk response.

4.4 Perturbation analysis

Three perturbations were considered: geometry perturbation δ_l, position perturbation δ_y, and non-Hermitian perturbation δ_γ. Disorder was sampled from normal distributions, as detailed in Section 11 of the Supplementary

Information. The two relevant resonance branches were tracked numerically and experimentally, and their frequency splitting was defined as $\Delta f = |f_1 - f_2|$. These measurements were used to compare the structural, BIC-symmetry-breaking, and exceptional-point responses.

Data availability

All data supporting the findings of this study are available within the main text and Supplementary Information. Additional data are available from the corresponding author upon request.

Acknowledgments

This work was supported by the National Natural Science Foundation of China (Grant No. 12474463), the National Key R&D Program of China (Grant No. 2022YFA1404400), the Scientific Research Innovation Capability Support Project for Young Faculty (Grant No. ZYGXQN JSKYCXNLZCXM-D8), the Fundamental Research Funds for the Central Universities, the Shanghai Pilot Program for Basic Research, the Xiaomi Young Talents Program, the State Key Laboratory of Mechanical System and Vibration (Grant No. MSV202603) and the China Postdoctoral Science Foundation.

Author contributions

Jiachen Meng: Investigation, Validation, Writing–original draft. Ruizhi Dong: Conceptualization, Methodology, Investigation, Validation, Writing–original draft, Writing–review and editing. Yihuan Zhu: Investigation, Validation. Xu Wang: Conceptualization, Investigation, Supervision, Writing–original draft, Writing–review and editing. Yong Li: Conceptualization, Supervision, Writing–review and editing.

Declarations

The authors declare no competing interests.

References

[1] Chiu, C.-K., Teo, J. C. Y., Schnyder, A. P. & Ryu, S. Classification of topological quantum matter with symmetries. *Reviews of Modern Physics* **88**, 035005 (2016).

[2] Ma, G., Xiao, M. & Chan, C. T. Topological phases in acoustic and mechanical systems. *Nature Reviews Physics* **1**, 281–294 (2019).

[3] Ozawa, T. *et al.* Topological photonics. *Reviews of Modern Physics* **91**, 015006 (2019).

[4] Gong, Z. *et al.* Topological phases of non-Hermitian systems. *Physical Review X* **8**, 031079 (2018).

[5] Shen, H., Zhen, B. & Fu, L. Topological band theory for non-Hermitian Hamiltonians. *Physical Review Letters* **120**, 146402 (2018).

[6] Yao, S. & Wang, Z. Edge states and topological invariants of non-Hermitian systems. *Physical Review Letters* **121**, 086803 (2018).

[7] Kunst, F. K., Edvardsson, E., Budich, J. C. & Bergholtz, E. J. Biorthogonal bulk–boundary correspondence in non-Hermitian systems. *Physical Review Letters* **121**, 026808 (2018).

[8] Kawabata, K., Shiozaki, K., Ueda, M. & Sato, M. Symmetry and topology in non-Hermitian physics. *Physical Review X* **9**, 041015 (2019).

[9] Bergholtz, E. J., Budich, J. C. & Kunst, F. K. Exceptional topology of non-Hermitian systems. *Reviews of Modern Physics* **93**, 015005 (2021).

[10] Bender, C. M. & Boettcher, S. Real spectra in non-Hermitian Hamiltonians having $\mathcal{PT}$ symmetry. *Physical Review Letters* **80**, 5243–5246 (1998).

[11] Heiss, W. D. The physics of exceptional points. *Journal of Physics A: Mathematical and Theoretical* **45**, 444016 (2012).

[12] El-Ganainy, R. *et al.* Non-Hermitian physics and $\mathcal{PT}$ symmetry. *Nature Physics* **14**, 11–19 (2018).

[13] Miri, M.-A. & Alù, A. Exceptional points in optics and photonics. *Science* **363**, eaar7709 (2019).

[14] Özdemir, S. K., Rotter, S., Nori, F. & Yang, L. Parity–time symmetry and exceptional points in photonics. *Nature Materials* **18**, 783–798 (2019).

[15] Ashida, Y., Gong, Z. & Ueda, M. Non-Hermitian physics. *Advances in Physics* **69**, 249–435 (2020).

[16] Peng, B. *et al.* Parity–time-symmetric whispering-gallery microcavities. *Nature Physics* **10**, 394–398 (2014).

[17] Wiersig, J. Enhancing the sensitivity of frequency and energy splitting detection by using exceptional points: Application to microcavity sensors for single-particle detection. *Physical Review Letters* **112**, 203901 (2014).

[18] Hodaei, H. *et al.* Enhanced sensitivity at higher-order exceptional points. *Nature* **548**, 187–191 (2017).

[19] Chen, W., Özdemir, S. K., Zhao, G., Wiersig, J. & Yang, L. Exceptional points enhance sensing in an optical microcavity. *Nature* **548**, 192–196 (2017).

[20] Langbein, W. No exceptional precision of exceptional-point sensors. *Physical Review A* **98**, 023805 (2018).

[21] Zhu, X., Ramezani, H., Shi, C., Zhu, J. & Zhang, X. $\mathcal{PT}$-symmetric acoustics. *Physical Review X* **4**, 031042 (2014).

[22] Fleury, R., Sounas, D. & Alù, A. An invisible acoustic sensor based on parity-time symmetry. *Nature Communications* **6**, 5905 (2015).

[23] Shi, C. *et al.* Accessing the exceptional points of parity-time symmetric acoustics. *Nature Communications* **7**, 11110 (2016).

[24] Ding, K., Ma, G., Zhang, Z. Q. & Chan, C. T. Experimental demonstration of an anisotropic exceptional point. *Physical Review Letters* **121**, 085702 (2018).

[25] Friedrich, H. & Wintgen, D. Interfering resonances and bound states in the continuum. *Physical Review A* **32**, 3231–3242 (1985).

[26] Hsu, C. W., Zhen, B., Stone, A. D., Joannopoulos, J. D. & Soljačić, M. Bound states in the continuum. *Nature Reviews Materials* **1**, 16048 (2016).

[27] Kodigala, A. *et al.* Lasing action from photonic bound states in continuum. *Nature* **541**, 196–199 (2017).

[28] Koshelev, K., Lepeshov, S., Liu, M., Bogdanov, A. & Kivshar, Y. Asymmetric metasurfaces with high-Q resonances governed by bound states in the continuum. *Physical Review Letters* **121**, 193903 (2018).

[29] Koshelev, K., Favraud, G., Bogdanov, A., Kivshar, Y. & Fratalocchi, A. Nonradiating photonics with resonant dielectric nanostructures. *Nanophotonics* **8**, 725–745 (2019).

[30] Lyapina, A. A., Maksimov, D. N., Pilipchuk, A. S. & Sadreev, A. F. Bound states in the continuum in open acoustic resonators. *Journal of Fluid Mechanics* **780**, 370–387 (2015).

[31] Sadreev, A. F. Interference traps waves in an open system: bound states in the continuum. *Reports on Progress in Physics* **84**, 055901 (2021).

[32] Zhen, B., Hsu, C. W., Lu, L., Stone, A. D. & Soljačić, M. Topological nature of optical bound states in the continuum. *Physical Review Letters* **113**, 257401 (2014).

[33] Bulgakov, E. N. & Maksimov, D. N. Topological bound states in the continuum in arrays of dielectric spheres. *Physical Review Letters* **118**, 267401 (2017).

[34] Qian, L., Zhang, W., Sun, H. & Zhang, X. Non-Abelian topological bound states in the continuum. *Physical Review Letters* **132**, 046601 (2024).

[35] Dong, R., Zhu, Y., Mao, D., Wang, X. & Li, Y. Observation of extreme anisotropic sensitivity at topological bound states in the continuum. *Physical Review Letters* **134**, 206601 (2025).

[36] Fan, H. *et al.* Acoustic non-Hermitian higher-order topological bound states in the continuum. *Applied Physics Letters* **126**, 071702 (2025).

[37] Luo, Y. & Sun, X. Topological bound states in the continuum in a non-Hermitian photonic system. *Nanophotonics* **14**, 43–50 (2025).

[38] Gao, H. *et al.* Non-Hermitian route to higher-order topology in an acoustic crystal. *Nature Communications* **12**, 1888 (2021).

[39] Gu, Z. *et al.* Topologically protected exceptional point with local non-Hermitian modulation in an acoustic crystal. *Physical Review Applied* **15**, 014025 (2021).

[40] Zhang, L. *et al.* Acoustic non-Hermitian skin effect from twisted winding topology. *Nature Communications* **12**, 6297 (2021).

[41] Zhao, H. *et al.* Non-Hermitian topological light steering. *Science* **365**, 1163–1166 (2019).

[42] Krasikova, M. *et al.* Acoustic bound states in the continuum in coupled Helmholtz resonators. *Physical Review Applied* **22**, 024045 (2024).

[43] Canós Valero, A., Sztranyovszky, Z., Muljarov, E. A., Bogdanov, A. & Weiss, T. Exceptional bound states in the continuum. *Physical Review Letters* **134**, 103802 (2025).

[44] Yu, R., Qi, X. L., Bernevig, B. A., Fang, Z. & Dai, X. Equivalent expression of $\mathbb{Z}_2$ topological invariant for band insulators using the non-Abelian Berry connection. *Physical Review B* **84**, 075119 (2011).

Supplementary Files

This is a list of supplementary files associated with this preprint. Click to download.

- TEPBICSM.pdf